



**HAL**  
open science

# A new non-colloidal suspension model A new rate-independent tensorial model for suspensions of non-colloidal rigid particles in Newtonian fluids

Olivier Ozenda, Pierre Saramito, Guillaume Chambon

## ► To cite this version:

Olivier Ozenda, Pierre Saramito, Guillaume Chambon. A new non-colloidal suspension model A new rate-independent tensorial model for suspensions of non-colloidal rigid particles in Newtonian fluids. 2017. hal-01528817v2

**HAL Id: hal-01528817**

**<https://hal.science/hal-01528817v2>**

Preprint submitted on 13 Jul 2017 (v2), last revised 24 Apr 2018 (v6)

**HAL** is a multi-disciplinary open access archive for the deposit and dissemination of scientific research documents, whether they are published or not. The documents may come from teaching and research institutions in France or abroad, or from public or private research centers.

L'archive ouverte pluridisciplinaire **HAL**, est destinée au dépôt et à la diffusion de documents scientifiques de niveau recherche, publiés ou non, émanant des établissements d'enseignement et de recherche français ou étrangers, des laboratoires publics ou privés.

# A new rate-independent tensorial model for suspensions of non-colloidal rigid particles in Newtonian fluids

O. Ozenda,<sup>1,2</sup> P. Saramito,<sup>1, a)</sup> and G. Chambon<sup>2</sup>

<sup>1)</sup>*Lab. J. Kuntzmann - CNRS and Grenoble university,  
CS 40700 - 38058 Grenoble cedex 9 - France*

<sup>2)</sup>*Grenoble Alpes University - IRSTEA - UR ETGR,  
2 rue de la Papeterie - St-Martin-d'Hères 38402 - France*

(Dated: 13 July 2017)

## Synopsis

We propose a new tensorial model to describe the rheology of non-colloidal suspensions. Qualitatively, this model proves capable of reproducing all the main non-Newtonian trends exhibited by concentrated suspensions: anisotropic and fore-aft asymmetric microstructure in simple shear and transient relaxation of the microstructure towards its stationary state. The model includes only few constitutive parameters, with clear physical meaning, that can be identified for comparisons with experimental data. Hence, quantitative predictions of the complex transient evolution of apparent viscosity observed after shear reversals are reproduced for a large range of volume fractions. Comparisons with micro-structural data shows that not only the depletion angle, but the pair distribution function, are well predicted. To our knowledge, it is the first time that a microstructure-based rheological model is successfully compared to such a wide experimental dataset.

## I. INTRODUCTION

Despite the apparent simplicity of the system, concentrated suspensions of non-colloidal, rigid spheres in a Newtonian fluid display a rich and complex rheological behavior (Stickel and Powell, 2005; Guazzelli and Morris, 2012; Denn and Morris, 2014). In the inertialess limit (zero Reynolds number), particle dynamics is essentially governed by hydrodynamic interactions since lubrication forces prevent, in principle, direct contacts. Linearity and reversibility of Stokes equation then lead to expect that the macroscopic behavior of the suspension should remain Newtonian. However, numerous experimental evidences showed the existence of non-Newtonian rheological effects as soon as the particle volume fraction  $\phi$  exceeds 0.2, typically. The most prominent examples include the development of normal stress differences in simple shear flow (Zarraga et al., 2000; Boyer et al., 2011b; Couturier et al., 2011; Dbouk et al., 2013), and the existence of transient viscosity drops upon reversal of the shearing direction (Gadala-Maria and Acrivos, 1980; Kolli et al., 2002; Blanc, 2011). There is nowadays a general agreement to relate these non-Newtonian effects to flow-induced changes in the microstructure of the suspension (Morris, 2009; Denn and Morris, 2014). The pair distribution function  $g(\mathbf{x})$ , i.e. the likelihood of finding pairs of particles at a separation vector  $\mathbf{x}$ , has been shown to become anisotropic and lose fore-aft symmetry under shear, with development of preferential concentration and depletion orientations that depend on the volume fraction  $\phi$  (Blanc et al., 2013). The asymmetry of the microstructure is the hallmark of a loss of reversibility of the system that, again, contradicts expectations based on Stokes equation. Although the precise mechanisms remain to be elucidated, it is generally interpreted as resulting from chaotic dynamics induced by the nonlinearity of the multi-body hydrodynamic interactions (Drazer et al., 2002), and/or from even weak perturbations of the hydrodynamic interactions by non-hydrodynamic near-contact forces (Metzger and Butler, 2010; Gallier et al., 2014). Note that the asymmetric microstructure, and the associated normal stresses, are also at the origin the cross-stream particle migration process observed

---

<sup>a)</sup>Electronic mail: [Pierre.Saramito@imag.fr](mailto:Pierre.Saramito@imag.fr)

in these suspensions when the shear rate is heterogeneous (Morris and Boulay, 1999; Miller et al., 2009).

Since the pioneering work of Einstein, most rheological models for suspensions assume an additive decomposition of the total Cauchy stress tensor  $\boldsymbol{\sigma}_{\text{tot}}$  into fluid and particle contributions (Einstein, 1906, 1956; Guazzelli and Morris, 2012). This decomposition naturally arises from mixture theories in which macroscopic quantities are obtained from averages over both phases (Jackson, 1997, 2000; Nott et al., 2011). While the fluid contribution is simply given by a Newtonian law (with the viscosity of the interstitial fluid), closure relations are needed to express the particle stresses. Schematically, two groups of models are found in the literature. The first group encompasses purely macroscopic approaches that do not contain explicit reference to the suspension microstructure, apart from the volume fraction  $\phi$ . The most popular representative of this class is the suspension balance model (SBM), introduced in 1994 by Nott and Brady (1994) (see also Morris and Boulay (1999); Miller and Morris (2006)), in which particle stresses are expressed as the sum of a shear and a normal term that are both linear in shear rate, with corresponding shear and normal viscosities given by empirical functions of  $\phi$ . By construction, SBM well reproduces experimental rheological measurements obtained in stationary shear. It also leads to realistic predictions concerning particle migration when the particle normal stresses are used as the driver of the migration flux, even if this approach has been questioned (Lhuillier, 2009; Nott et al., 2011). However, as a counterpart for its simplicity, this model is devoid of any time scale and therefore unable to account for transients observed during shear reversal experiments. In addition, earlier versions were not invariant by changes of reference frame, although an ad hoc frame-invariant extension has been proposed (Miller et al., 2009).

In the second group of models, particle stress is made explicitly dependent on the microstructure through the consideration of a local *conformation tensor* that is inspired from the orientation distribution tensor defined for dilute fiber suspensions (see e.g. Lipscomb et al. (1988); Reddy and Mitchell (2001)). The conformation tensor, denoted  $\mathbf{b}_e$  in this paper, is a second order symmetric positive definite tensor describing micro-structure anisotropy. Hand (1962) formulated a general representation theorem for the total Cauchy stress tensor  $\boldsymbol{\sigma}_{\text{tot}}$  in term of the conformation tensor  $\mathbf{b}_e$  and the deformation rate  $D(\mathbf{u}) = (\nabla\mathbf{u} + \nabla\mathbf{u}^T)/2$ , where  $\mathbf{u}$  is the velocity field of the suspension. This general representation should be closed by a constitutive equation for the evolution of the conformation tensor. An important constraint is that the characteristic time associated to the conformation tensor  $\mathbf{b}_e$ , representing the microstructure evolution, must scale inversely with the deformation rate  $|D(\mathbf{u})|$  in order to ensure strain-scaling and *rate-independence* of the transients, as observed experimentally (see e.g. Blanc (2011)) and imposed by dimensional analysis (Brady and Morris, 1997; Goddard, 2006). Note that the rate-independence constraint leads to constitutive equations that are similar to hypo-elastic models (see e.g. Kolymbas (1991)). For concentrated suspensions of spherical particles, Phan-Thien (1995) proposed a differential constitutive equation for the conformation tensor, that led to prediction qualitatively in agreement with time-dependent experimental observations in shear reversal (Gadala-Maria and Acrivos, 1980; Kolli et al., 2002; Narumi et al., 2002). The structural unit used to define the conformation tensor was taken as the vector joining two neighboring particles, thereby encoding a direct connection with the pair distribution function  $g(\mathbf{x})$ . Later, Phan-Thien et al. (1999, 2000) went further with a micro-macro model inspired from statistical mechanics for the constitutive equation of the conformation tensor, but no quantitative comparisons were obtained. In 2006, Goddard (2006) revisited this approach, and proposed a model involving twelve material parameters and two tensors for describing the anisotropy. By a systematic fitting procedure of the parameters, he obtained numerical results in quantitative agreement with shear reversal experiments (Kolli et al., 2002; Narumi et al., 2002). Also in 2006, Stickel et al. (2006) (see also Stickel et al. (2007); Yapici et al. (2009)) defined the conformation tensor on the base of particle mean free path, and simplified the expression of the stress to be linear in the deformation rate and the conformation tensor. Their model nevertheless also involves 13 free parameters. These authors obtained numerical results in qualitative agreement with a shear reversal experiment (Kolli et al., 2002; Narumi et al., 2002) but failed to obtain

quantitative comparisons. In contrast with SBM model, all these tensorial models are, by construction, frame-invariant and potentially applicable to arbitrary flow geometries and conditions. As for polymer models, normal stress differences naturally arise from the use of some objective derivative of the conformation tensor  $\mathbf{b}_e$  (see Saramito (2016)). The time-dependent relaxation of this tensor, representing microstructure evolution, leads to transient responses when the loading is varied. Nevertheless, these microstructure-based models are still rather complex, and the identification of parameters is generally not obvious.

This paper is a contribution to an ongoing effort for the development of more tractable microstructure-based rheological models. With the least number of adjustable parameters, the proposed model is relatively simple, yet capable of accounting both for the macroscopic non-Newtonian rheological features of non-colloidal suspensions and for the rate-independent evolution of the microstructure. In particular, this model is able to describe the experimentally observed anisotropic effects expressed by the pair-distribution function. It also qualitatively and quantitatively agrees, for a wide range of volume fraction, with experimental data for time-dependent shear reversals.

The outline of the paper is as follows. The second section presents the model statement while the third one turns to validation with experimental data for the microstructure anisotropy and depletion angle in stationary shear. Section 4 deals with time dependent flows, specifically shear reversals, and present some comparisons with experiments for the apparent viscosity. Finally, the last section develops a discussion and a conclusion.

## II. MATHEMATICAL MODEL

### A. Rheological model

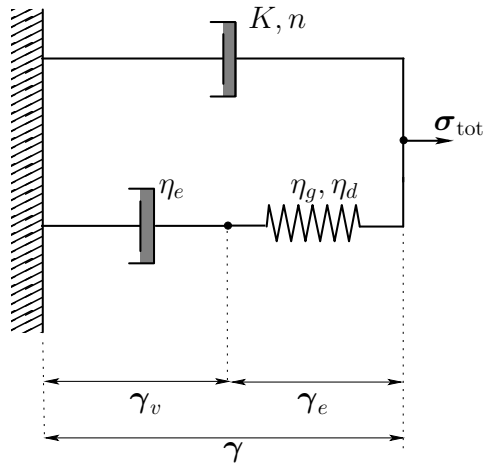


**FIG. 1.** Schematic diagram of the rheological model: link between the total stress  $\sigma_{\text{tot}}$  and the total deformation  $\gamma = \gamma_e + \gamma_v$ .

Our model is inspired by the simple rheological diagram represented in Fig. 1. Let  $\gamma$  denote the tensor of the total deformation of the suspension. We assume that it can be decomposed as the sum of a reversible deformation  $\gamma_e$  and an irreversible one  $\gamma_v$ :

$$\gamma = \gamma_e + \gamma_v \quad (1)$$

The reversible deformation  $\gamma_e$  can be interpreted as the deformation of instantaneous microstructural units constituted by neighboring particles, that we shall call *particle clusters* (Fig. 2), while the irreversible deformation  $\gamma_v$  is due to global rearrangements of neighboring particles through viscous flow. We introduce the *conformation* tensor  $\mathbf{b}_e = \mathbf{I} + \gamma_e$ . This

tensor measures the anisotropy of the particle clusters, as shown on Fig. 2. In the case of an isotropic distribution of particles, we have both  $\gamma_e = 0$  and  $\mathbf{b}_e = \mathbf{I}$ .

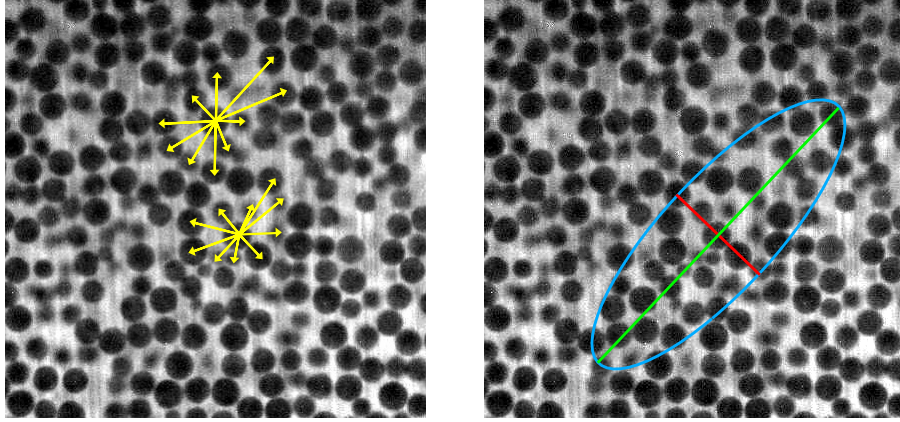


**FIG. 2.** (left) Particle *clusters* represented by links between neighboring particles. (right) Representation of the local microstructure by a conformation tensor  $\mathbf{b}_e = \mathbf{I} + \gamma_e$ . This tensor is represented by an ellipse. The compression axis is in red and the dilatation axis in green. Background photography from Blanc (2011), Fig. 4.7 with  $\phi = 0.55$ .

The next step is to obtain a constitutive equation for the cluster deformation  $\gamma_e$ . We define the *cluster stress*, denoted as  $\boldsymbol{\tau}$ , which expresses the contribution of microstructure anisotropy to the total stress of the suspension. This cluster stress  $\boldsymbol{\tau}$  is related to the rate of irreversible deformation  $\dot{\gamma}_v$  through:

$$\boldsymbol{\tau} = \eta_e \dot{\gamma}_v \quad (2)$$

where  $\eta_e \geq 0$  is an associated viscosity. Moreover, we assume a non-linear relation between  $\boldsymbol{\tau}$  and the cluster deformation  $\gamma_e$ :

$$\boldsymbol{\tau} = \eta_g |\dot{\gamma}| \gamma_e + \eta_d (\dot{\gamma} : \gamma_e) \gamma_e \quad (3)$$

The first term on the right-hand-side, linear with respect to  $\gamma_e$ , involves a factor  $\eta_g |\dot{\gamma}|$  that is interpreted as a rate-dependent elastic modulus. Here,  $\eta_g$  is a constant coefficient with the dimension of a viscosity. The second term on the right-hand side of (3), quadratic with respect to  $\gamma_e$ , writes equivalently  $\eta_d (\gamma_e \otimes \gamma_e) : \dot{\gamma}$ . Such quadratic expressions in  $\gamma_e \otimes \gamma_e$  commonly derive from the closure of a fourth-order structure tensor in statistical micro-macro models for spherical or fiber suspensions (see e.g. Lipscomb et al. (1988); Reddy and Mitchell (2001)). It involves an additional constant  $\eta_d$  with the dimension of a viscosity. Differentiating (1), replacing  $\dot{\gamma}_v$  from (2) and using (3), the following constitutive equation is obtained for  $\gamma_e$ :

$$\dot{\gamma}_e + \alpha |\dot{\gamma}| \gamma_e + \beta (\dot{\gamma} : \gamma_e) \gamma_e = \dot{\gamma}$$

where  $\alpha = \eta_g / \eta_e$  and  $\beta = \eta_d / \eta_e$  are dimensionless parameters. The time derivative  $\dot{\gamma}_e$  is given by the upper-convected tensor derivative, denoted hereafter  $\mathcal{D}\gamma_e / \mathcal{D}t$  (see e.g. Saramito (2016), chap 4):

$$\frac{\mathcal{D}\gamma_e}{\mathcal{D}t} = \frac{\partial \gamma_e}{\partial t} + (\mathbf{u} \cdot \nabla) \gamma_e - \nabla \mathbf{u} \gamma_e - \gamma_e \nabla \mathbf{u}^T$$

The term  $\dot{\gamma}$  is identified to two times the deformation rate tensor  $D(\mathbf{u}) = (\nabla \mathbf{u} + \nabla \mathbf{u}^T) / 2$ . The constitutive equation for  $\gamma_e$  thus becomes:

$$\frac{\mathcal{D}\gamma_e}{\mathcal{D}t} + \{\alpha |2D(\mathbf{u})| + 2\beta (D(\mathbf{u}) : \gamma_e)\} \gamma_e = 2D(\mathbf{u}) \quad (4)$$

This equation can be seen as a rate-independent variant of a viscoelastic Oldroyd (1950) differential constitutive equation with an additional quadratic term. The corresponding rheological diagram is represented on Fig. 1.

Finally, the total Cauchy stress tensor of the suspension writes (Fig. 1):

$$\boldsymbol{\sigma}_{\text{tot}} = -p_f \mathbf{I} + 2K |2D(\mathbf{u})|^{n-1} D(\mathbf{u}) + 2\eta_e \{ \alpha |D(\mathbf{u})| + \beta (D(\mathbf{u}) : \boldsymbol{\gamma}_e) \} \boldsymbol{\gamma}_e \quad (5)$$

The first term involves  $p_f$ , the pressure in the fluid phase. The second term represents the base viscosity of the suspension, expressed here by a power law function, where  $K$  and  $n$  are material parameters, to account for possible shear-thinning as observed in some laboratory experiments (Gadala-Maria and Acrivos, 1980; Blanc, 2011). The third term represents the cluster stress  $\boldsymbol{\tau}$ . Note that the stress decomposition underlying (5) differs from the classical decomposition between fluid and particle stresses used in most suspension models. Here, we have chosen to separate between the stresses that would be observed for an isotropic microstructure (the *base* viscosity), and the stresses induced by the anisotropic arrangement of the microstructure (represented by  $\boldsymbol{\tau}$ ). Roughly, the first contribution should account more for long-range hydrodynamic interactions between particles, while the second one should account for short-range, hydrodynamic and contact, interactions. As a consequence, we expect all the parameters of the model, including  $K$  (and possibly also  $n$ ), to depend on volume fraction  $\phi$ .

## B. Problem statement

Coupling the above constitutive equation with the mass and momentum conservation equations of the mixture, the problem can be formulated as a system of three equations and three unknowns:  $\boldsymbol{\gamma}_e$ , the particle clusters deformation;  $\mathbf{u}$ , the mixture velocity; and  $p_f$ , the pressure in the fluid phase:

$$\frac{\mathcal{D}\boldsymbol{\gamma}_e}{\mathcal{D}t} + \{ \alpha |2D(\mathbf{u})| + 2\beta (D(\mathbf{u}) : \boldsymbol{\gamma}_e) \} \boldsymbol{\gamma}_e - 2D(\mathbf{u}) = 0 \quad (6a)$$

$$\rho \frac{D\mathbf{u}}{Dt} + \text{div} \{ -p_f \mathbf{I} + 2K |2D(\mathbf{u})|^{n-1} D(\mathbf{u}) + \alpha \eta_e |2D(\mathbf{u})| \boldsymbol{\gamma}_e + 2\beta \eta_e (D(\mathbf{u}) : \boldsymbol{\gamma}_e) \boldsymbol{\gamma}_e \} = \rho \mathbf{g} \quad (6b)$$

$$\text{div } \mathbf{u} = 0 \quad (6c)$$

The incompressibility relation (6c) is a consequence of mass conservation of the fluid and solid phases. From a mathematical point of view, the fluid pressure  $p_f$  acts as a Lagrange multiplier associated to this incompressibility constraint. The problem is closed by suitable initial and boundary conditions. In (6b),  $D/Dt = \partial/\partial t + \mathbf{u} \cdot \nabla$  denotes the Lagrange derivative and  $\rho$  is the density of the mixture. From Hulsen (1990), it is possible to show that the constitutive equation (6a) leads to a conformation tensor  $\mathbf{b}_e = \mathbf{I} + \boldsymbol{\gamma}_e$  that is always positive definite. Note that the volume fraction  $\phi$ , and hence  $\rho$ , are supposed to be constant during the flow: in agreement with experimental evidences (Denn and Morris, 2014), we assume the time scale for migration to be large compared to the typical time scales for microstructure evolution, and focus on the short-time response of the suspension. Otherwise, the system could be also coupled with an additional diffusion equation for the volume fraction (see e.g. Miller and Morris (2006)).

## III. STATIONARY SHEAR FLOWS AND MICROSTRUCTURE ANISOTROPY

Let us consider a simple shear flow. The  $x$  axis is in the flow direction and the  $y$  axis in the direction of the gradient  $\nabla = (0, \partial_y, 0)$ . Let  $\mathbf{u}(t, x, y, z) = (u_x(t, y), 0, 0)$  be the velocity and  $\dot{\gamma}(t) = \partial_y u_x$  be the spatially uniform shear rate. The constitutive equations (4)-(5) become,

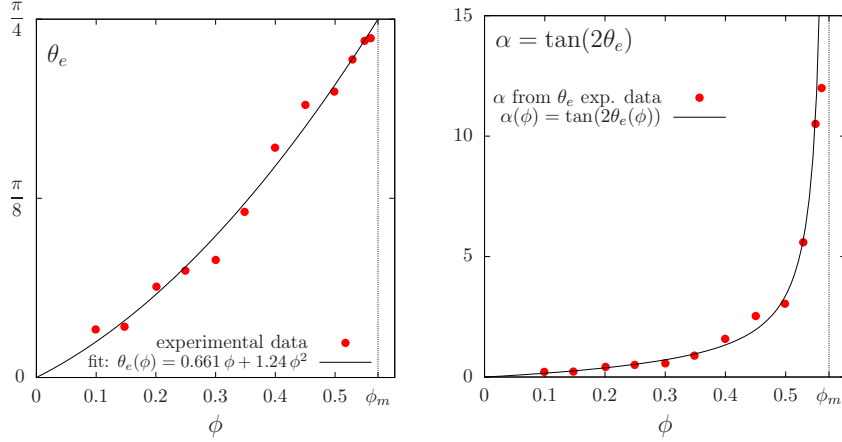


**FIG. 3.** (left) Depletion angle  $\theta_e$  versus volume fraction  $\phi$ : experimental data from [Blanc \(2011\)](#), Fig. 5.11 and best fit with a second order polynomial. (right) Dependence upon  $\phi$  of model parameter  $\alpha$ .

after expanding the upper-convected derivative (see e.g. [Saramito \(2016\)](#), chap 4):

$$\partial_t \gamma_{e,xy} + \alpha |\dot{\gamma}| \gamma_{e,xy} = \dot{\gamma} \quad (7a)$$

$$\partial_t \gamma_{e,xx} - 2\dot{\gamma} \gamma_{e,xy} + \alpha |\dot{\gamma}| \gamma_{e,xx} = 0 \quad (7b)$$

$$\partial_t \gamma_{e,yy} + \alpha |\dot{\gamma}| \gamma_{e,yy} = 0 \quad (7c)$$

$$\partial_t \gamma_{e,zz} + \alpha |\dot{\gamma}| \gamma_{e,zz} = 0 \quad (7d)$$

$$\sigma_{xy} = \alpha \eta_e |\dot{\gamma}| \gamma_{e,xy} + \beta \eta_e \dot{\gamma} \gamma_{e,xy}^2 + K |\dot{\gamma}|^{n-1} \dot{\gamma} \quad (7e)$$

$$\sigma_{xx} = \alpha \eta_e |\dot{\gamma}| \gamma_{e,xx} + \beta \eta_e \dot{\gamma} \gamma_{e,xy} \gamma_{e,xx} \quad (7f)$$

completed by an initial condition for  $\gamma_e$ . Remark that, in (7a)-(7d), the quadratic term with the  $\beta$  factor in (4) has been omitted for simplicity. Also, for simplicity, we assume an isotropic microstructure at  $t = 0$ . Hence,  $\gamma_{e,yy}(0) = \gamma_{e,zz}(0) = 0$ , which yields  $\gamma_{e,yy}(t) = \gamma_{e,zz}(t) = 0$  for all  $t > 0$ . Similarly,  $\gamma_{e,xz}(0) = \gamma_{e,yz}(0) = 0$ .

We first focus on a stationary simple shear flow where the shear rate is supposed to be constant and is denoted by  $\dot{\gamma}_0$ . In that case, the solution writes explicitly:

$$\gamma_{e,xy} = \text{sgn}(\dot{\gamma}_0) \alpha^{-1}, \quad \gamma_{e,xx} = 2\alpha^{-2} \quad (8a)$$

$$\sigma_{xy} = (K |\dot{\gamma}_0|^{n-1} + (1 + \beta \alpha^{-2}) \eta_e) \dot{\gamma}_0 \quad (8b)$$

$$\sigma_{xx} = 2\alpha^{-1} (1 + \beta \alpha^{-2}) \eta_e |\dot{\gamma}_0| \quad (8c)$$

Observe that the model is able to predict a normal stress component proportional to the shear rate  $|\dot{\gamma}_0|$ . This feature is in agreement with many experimental observations (see e.g. [Zarraga et al. \(2000\)](#)). The particle pressure is defined by  $p_p = \text{tr}(\boldsymbol{\tau})/3$ . For the present stationary simple shear flow, we have:

$$p_p = (2/3) \alpha^{-1} (1 + \beta \alpha^{-2}) \eta_e |\dot{\gamma}_0|$$

and thus,  $p_p$  is also proportional to the shear rate  $|\dot{\gamma}_0|$ . This feature has also been experimentally observed by [Deboeuf et al. \(2009\)](#). Note that, when  $n = 1$ , the shear stress component  $\sigma_{xy}$  also scales linearly with  $\dot{\gamma}_0$ .

Let us now turn to microstructural aspects, described by the particle cluster deformation tensor  $\gamma_e$ . From (8a), the eigenvector associated to the largest eigenvalue of the tensor  $\gamma_e$ ,



makes an angle with the  $x$  axis denoted as  $\theta_e$ , and are given by:

$$\begin{aligned} \theta_e &= \operatorname{atan}\left(\frac{-1 + \sqrt{1 + \alpha^2}}{\alpha}\right) = \frac{1}{2}\operatorname{atan}(\alpha) \\ \iff \alpha &= \tan(2\theta_e) \end{aligned} \quad (9)$$

As  $\mathbf{b}_e = \mathbf{I} + \boldsymbol{\gamma}_e$ , the tensors  $\mathbf{b}_e$  and  $\boldsymbol{\gamma}_e$  share the same eigensystem. The angle  $\theta_e$  is thus also associated to largest eigenvalue of  $\mathbf{b}_e$ , i.e. to the dilation direction of the microstructure: in this direction, the probability to find two particles in contact is the smallest, and  $\theta_e$  is called the *depletion angle*. Experimental data for the depletion angle  $\theta_e$  versus volume fraction  $\phi$  are presented in Blanc (2011), Fig. 5.11 and are reproduced on Fig. 3 (left), together with a best fit using a second order polynomial denoted by  $\theta_e(\phi)$ . Assuming  $\theta_e(0) = 0$  and  $\theta_e(\phi_m) = \pi/4$ , with  $\phi_m$  the maximum volume fraction of the suspension, the second order polynomial template can be expressed as:

$$\theta_e(\phi) = \delta_e \phi + \left(\frac{\pi}{4} - \delta_e \phi_m\right) \left(\frac{\phi}{\phi_m}\right)^2 \quad (10)$$

where  $\phi_m = 0.571$  and  $\delta_e = 0.661$  are adjusted through nonlinear least square method, as implemented by Williams and Keley (2010).

Through (9), the dependence upon  $\phi$  of the  $\alpha$  parameter of the present model is thus directly deduced from the experimental data (see Fig. 3, right):

$$\alpha(\phi) = \tan(1.32\phi + 2.48\phi^2) \quad (11)$$

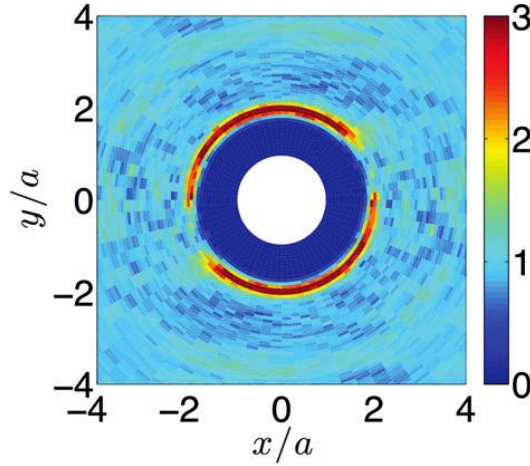


FIG. 4. Pair distribution function  $g(x, y)$ : experimental observation by Blanc et al. (2013) for a stationary shear flow with  $\phi = 0.35$  and where  $a$  denotes the radius of the particles.

Fig. 4 represents, for a suspension at  $\phi = 0.35$  submitted to a stationary shear flow, the pair distribution function  $g(\mathbf{x})$  in the shear plane  $(x, y)$ . This result has been obtained from experimental data through image processing (Blanc et al., 2013). Recall that  $g(\mathbf{x})$  is the conditional probability, when there is already a particle in  $\mathbf{x}_0 = 0$ , to find a particle at any location  $\mathbf{x} \in \mathbb{R}^2$ , normalized by the average particle density  $\phi/(4\pi a^3/3)$ , where  $a$  is particle radius. Observe on Fig. 4 that  $g$  is zero in the central circle of diameter  $2a$ , due to non-penetration of particles. It is maximum in a thin band  $[2a, 2a + \delta]$  corresponding to near-contact, and then tends to 1 when the distance increases. We switch to polar coordinates  $(r, \theta)$  in the shear plane and, in order to simplify the modeling of this function, we assume that  $g$  does not depend upon  $r$  in this band, but depends only upon  $\theta$ . Thus,



we introduce its average value, denoted as  $\tilde{g}(\theta)$ , in radial direction in the thin band, and the associated probability distribution function  $p(\theta)$  such that

$$p(\theta) = \frac{\tilde{g}(\theta)}{\int_{-\pi}^{\pi} \tilde{g}(\theta) d\theta}$$

Note that it is interpreted as the probability to find, for each particle in the suspension, a neighboring particle in the  $\theta$  direction inside the thin band. We then introduce the following averaging operator, denoted as  $\langle \cdot \rangle$ , defined for any function  $\varphi(\theta)$  by:

$$\langle \varphi \rangle = \int_{-\pi}^{\pi} \varphi(\theta) p(\theta) d\theta \quad (12)$$

Let  $\boldsymbol{\ell} = \boldsymbol{x} - \boldsymbol{x}_0$  denotes the separation between two neighboring particles  $\boldsymbol{x}$  and  $\boldsymbol{x}_0$  (defined such that there is no other particles between them). Assuming that the probability to find a neighbor particle outside the thin band is negligible, we define the *texture* tensor  $\langle \boldsymbol{\ell} \otimes \boldsymbol{\ell} \rangle$  at  $\boldsymbol{x}_0$  by:

$$\begin{aligned} \langle \boldsymbol{\ell} \otimes \boldsymbol{\ell} \rangle &= \int_{r=2a}^{r=2a+\delta} \int_{\theta=-\pi}^{\theta=\pi} \boldsymbol{\ell} \otimes \boldsymbol{\ell} p(\theta) r dr d\theta \\ &= \int_{r=2a}^{r=2a+\delta} r^3 dr \int_{\theta=-\pi}^{\theta=\pi} \boldsymbol{n} \otimes \boldsymbol{n} p(\theta) d\theta \\ &= c_{a,\delta} \langle \boldsymbol{n} \otimes \boldsymbol{n} \rangle \end{aligned} \quad (13)$$

where  $\boldsymbol{n}(\theta) = (\cos \theta, \sin \theta)$  is the unit outward normal vector to the unit circle and  $c_{a,\delta}$  is a constant that depends only upon  $a$  and  $\delta$ . We recognize the *fabric* tensor  $\langle \boldsymbol{n} \otimes \boldsymbol{n} \rangle$  widely used in many contexts, such as granular medias, fiber suspensions and liquid crystals, as a description of anisotropy. Observe that

$$\text{tr} \langle \boldsymbol{n} \otimes \boldsymbol{n} \rangle = \int_{-\pi}^{\pi} p(\theta) d\theta = 1 \quad (14)$$

as  $p$  is a distribution of probability. We assume that the conformation tensor  $\boldsymbol{b}_e = \boldsymbol{I} + \boldsymbol{\gamma}_e$ , which describes the anisotropy of the flowing suspension, should be proportional to both  $\langle \boldsymbol{\ell} \otimes \boldsymbol{\ell} \rangle$  and  $\langle \boldsymbol{n} \otimes \boldsymbol{n} \rangle$ . Taking into account that  $\langle \boldsymbol{n} \otimes \boldsymbol{n} \rangle$  has trace equal to one, we simply take:

$$\langle \boldsymbol{n} \otimes \boldsymbol{n} \rangle = \frac{\boldsymbol{b}_e}{\text{tr} \boldsymbol{b}_e} \quad (15)$$

From (15), the first Fourier mode of  $p(\theta)$  can be expressed explicitly in terms of the parameter  $\alpha$  and the depletion angle  $\theta_e$ : see appendix A, relation (A3). This prediction is compared on Fig. 5 with experimental data from Blanc (2011), Figs. 5.9 and 5.10. Observe that both predicted (in black) and experimental (in dotted-red) curves present two main lobes, separated by the depletion angle direction. The raw experimental probability distribution, represented by the point-dotted red curve, is perturbed by higher-frequency modes. These high frequency modes are potentially very sensitive to both experimental errors from image preprocessing and the choice of the width of the thin band  $[a, a + \delta]$  used to integrate the pair distribution function, as pointed out by Blanc (2011), Fig. 5.6. The truncated Fourier series expansion of experimental data, up to the first order, is represented by the thin red dotted line on Fig. 5: Observe that the noise is then removed and remark the good agreement between the model prediction and the filtered data.

Fig. 6 represents the five first Fourier coefficients of the experimental data. Observe the rapid decrease of these coefficients, as expected. When the volume fraction  $\phi$  becomes close to the maximal fraction  $\phi_m$ , the second mode dominates. A similar behavior has already been experimentally observed for dry granular material Troadec et al. (2002) and can be explained by steric exclusion of neighbors. This second Fourier mode cannot be determined by the present model, as explained in appendix A.

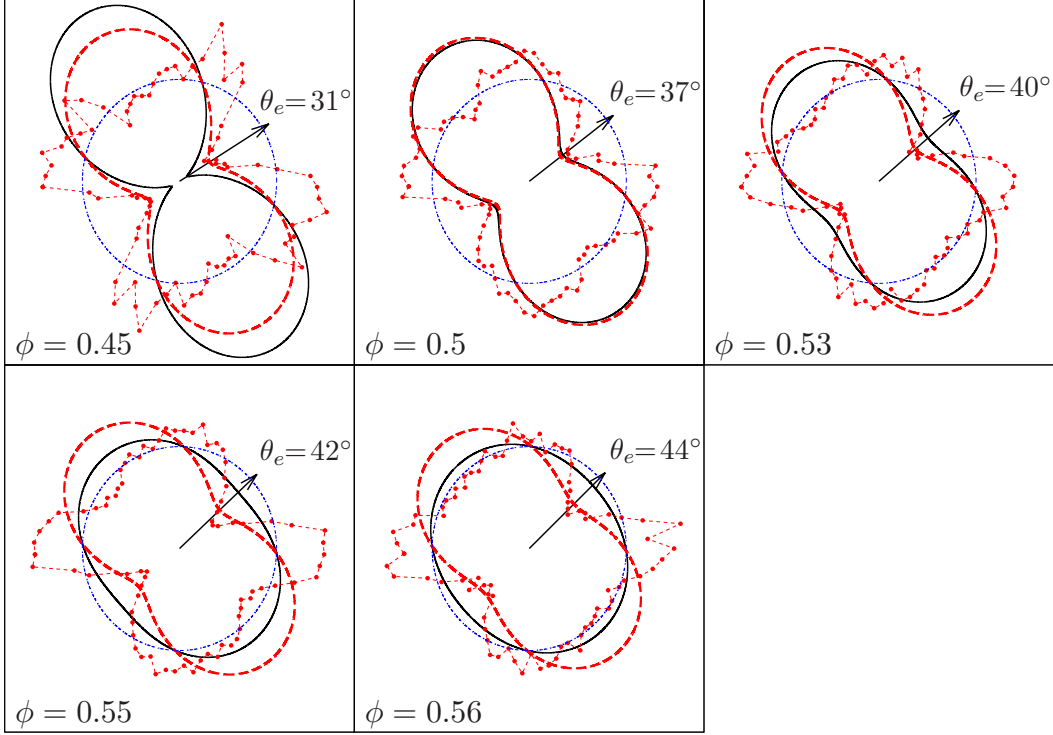


**FIG. 5.** Probability distribution function  $p(\theta)$ , represented in polar coordinates as  $r = p(\theta)$ . Comparison between model prediction (black curve) and experimental data (red points-dotted-curves) by Blanc (2011), Fig. 5.10. The red dotted-line corresponds to a truncated Fourier expansion of experimental data up to the first order. The depletion angle is indicated by an arrow and its value is given in degrees. The dotted blue circle represents the equiprobable (isotropic) distribution  $p(\theta) = 1/(2\pi)$ .

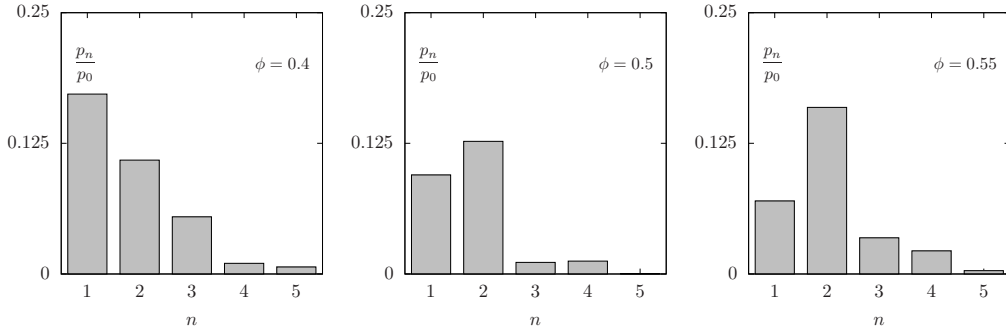


**FIG. 6.** Five first Fourier coefficients  $p_k$ ,  $k \geq 1$  of the probability distribution function  $p(\theta)$ , from experimental data by Blanc (2011), Fig. 5.10, for  $\phi = 0.4, 0.5$  and  $0.55$  from left to right.

#### IV. TIME-DEPENDENT SIMPLE SHEAR FLOWS

##### A. Shear startup, reversal and pause

For simple shear flows, the problem reduces to the time-dependent linear system of ordinary differential equation (7a)-(7f). For a constant applied shear rate  $\dot{\gamma}_0$ , the system can be

explicitly solved by performing the change of variable  $\gamma = |\dot{\gamma}_0|t$ , where  $\gamma$  represents the deformation. The solution writes:

$$\gamma_{e,xy}(\gamma) = (1 - e^{-\alpha\gamma}) \operatorname{sgn}(\dot{\gamma}_0)\alpha^{-1} + e^{-\alpha\gamma}\gamma_{e,xy}(0) \quad (16a)$$

$$\gamma_{e,xx}(\gamma) = (1 - e^{-\alpha\gamma}) 2\alpha^{-2} + e^{-\alpha\gamma}\{\gamma_{e,xx}(0) + 2\gamma(\operatorname{sgn}(\dot{\gamma}_0)\gamma_{e,xy}(0) - \alpha^{-1})\} \quad (16b)$$

and then, the total tress tensor  $\boldsymbol{\sigma}_{\text{tot}}$  is explicitly given by (7e)-(7f).

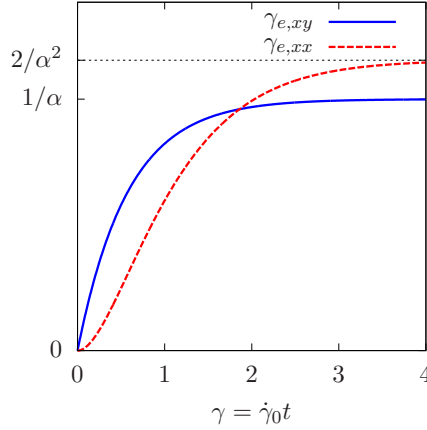


**FIG. 7.** Shear startup from rest: exponential relaxation of the  $\gamma_e$  tensor components versus shear deformation  $\gamma = \dot{\gamma}_0 t$  (with  $\alpha = \sqrt{3}$ ).

For a startup from a material at rest at  $t = 0$  with an isotropic microstructure, we have  $\gamma_e(0) = 0$ . If a constant shear rate  $\dot{\gamma}_0 > 0$  is imposed when  $t > 0$ , the solution (16a)-(16b) becomes:

$$\begin{aligned} \gamma_{e,xy}(\gamma) &= (1 - e^{-\alpha\gamma}) \alpha^{-1} \\ \gamma_{e,xx}(\gamma) &= (1 - e^{-\alpha\gamma}) 2\alpha^{-2} - e^{-\alpha\gamma} 2\alpha^{-1}\gamma \end{aligned}$$

As shown on Fig. 7, the solution displays an exponential relaxation towards the steady state solution. Remark that the graph of the solution versus the shear deformation  $\gamma = \dot{\gamma}_0 t$ , is invariant when changing the value of shear rate  $\dot{\gamma}_0 > 0$ . This is a fundamental property of rate-independent materials.

Let us now turn to a case of shear reversal: the material is first sheared with a negative shear rate  $-\dot{\gamma}_0$  until a first stationary regime is reached. Then, at  $t = 0$ , the shear rate is suddenly reversed to the opposite value  $+\dot{\gamma}_0 > 0$ . In that case,  $\gamma_{e,xy}(0) = -\alpha^{-1}$ ,  $\gamma_{e,xx}(0) = 2\alpha^{-2}$  and the solution (16a)-(16b) becomes:

$$\begin{aligned} \gamma_{e,xy}(\gamma) &= (1 - 2e^{-\alpha\gamma}) \alpha^{-1} \\ \gamma_{e,xx}(\gamma) &= (1 - e^{-\alpha\gamma}) 2\alpha^{-2} + e^{-\alpha\gamma}(2\alpha^{-2} - 4\alpha^{-1}\gamma) \end{aligned}$$

As shown on Fig. 8, at  $t = 0$ , the particle clusters, represented by the conformation tensor  $\mathbf{b}_e = \mathbf{I} + \boldsymbol{\gamma}_e$  as an ellipse, start to rotate towards a symmetrically opposite position. According to (9), the depletion angle increases from  $\theta_e(0) = -\operatorname{atan}(\alpha)/2$  at  $t = 0$  to reach asymptotically its new value  $\theta_e(\infty) = +\operatorname{atan}(\alpha)/2$ . With the choice  $\alpha = \sqrt{3}$  made in Fig. 8, we have  $\theta_e(\infty) = \pi/6$ . The depletion angle is expressed at any  $\gamma = \dot{\gamma}_0 t$  from the  $\gamma_e$  tensor components by:

$$\theta_e(\gamma) = \operatorname{atan} \left( \frac{-\gamma_{e,xx}(\gamma) + \sqrt{\gamma_{e,xx}^2(\gamma) + 4\gamma_{e,xy}^2(\gamma)}}{\gamma_{e,xy}(\gamma)} \right)$$

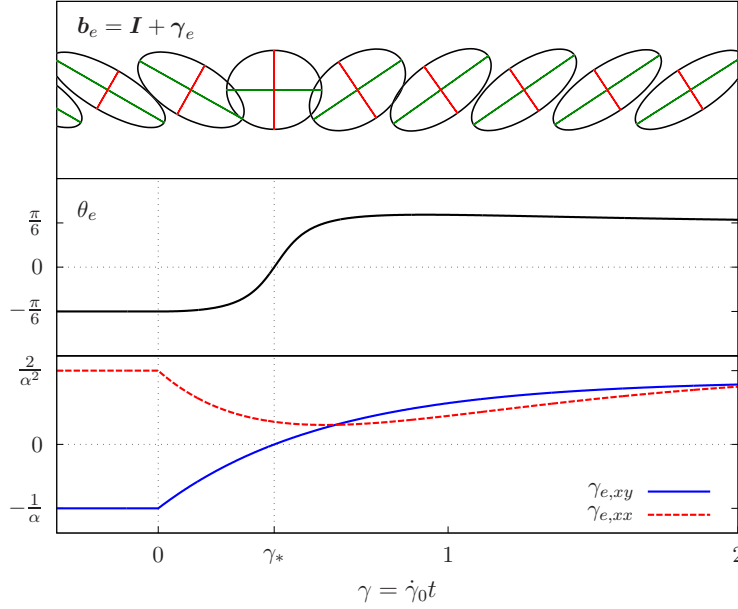


**FIG. 8.** Shear reversal at  $t = 0$ : evolution versus shear deformation  $\gamma = \dot{\gamma}_0 t$  of the conformation tensor  $\mathbf{b}_e = \mathbf{I} + \gamma_e$  represented as an ellipse. Eigenvector associated to compression (resp. dilation), i.e. to the smallest (resp. largest) eigenvalue of  $\mathbf{b}_e$ , is represented in red (resp. green). On the bottom, plots for the depletion angle  $\theta_e(t)$ , and the  $\gamma_e$  tensor components versus shear deformation  $\gamma = \dot{\gamma}_0 t$ . (Parameter  $\alpha$  is taken as  $\sqrt{3}$  in this plot.)

A Taylor development for small  $\gamma_{e,xy}(\gamma)$  shows that  $\theta_e(\gamma)$  vanishes when  $\gamma_{e,xy}(\gamma) = 0$ , i.e. when the shear deformation is equal to the critical value  $\gamma_* = \alpha^{-1} \log(2)$ . For this critical deformation, the ellipse axis associated to the largest eigenvalue (in green on Fig. 8), is horizontal with  $\gamma_{e,xy}(\gamma_*) = 0$  and  $\gamma_{e,xx}(\gamma_*) = 2(1 - \log(2))\alpha^{-2} > 0$ . It means that the particle cluster temporarily presents a fore-aft symmetry structure, but the cluster structure is not isotropic, i.e.  $\mathbf{b}_e \neq \mathbf{I}$  when  $\gamma = \gamma_*$ .

For a general  $\dot{\gamma}(t)$  evolution, the system of ordinary differential equations (7a)-(7f) is solved using the `lsode` library (Radhakrishnan and Hindmarsh, 1993), as interfaced in the `octave` software (Eaton et al., 2011). Fig. 9 plots the response in stress components and depletion angle when applying a succession of startups and reversals, possibly separated by pauses. In agreement with experimental observations (see Kolli et al. (2002), Fig. 3), when the imposed shear rate changes from  $\dot{\gamma}_0 \neq 0$  to zero, i.e. during a pause, both the particle pressure  $p_p = \text{tr}(\boldsymbol{\tau})/3 = \tau_{xx}/3$  and the shear stress  $\sigma_{xy}$  instantaneously fall to zero. Observe however that the depletion angle remains constant during the pause: the microstructure is conserved. This latter feature can be deduced from the constitutive equation (4), which simply reduces to  $\mathcal{D}\gamma_e/\mathcal{D}t = 0$  when the shear rate is zero. After a pause, if the shear restarts suddenly in the same direction, experimental observations (see Kolli et al. (2002), Fig. 3) showed that both the the particle pressure  $p_p = \tau_{xx}/3$  and the shear stress  $\sigma_{xy}$  jump instantaneously to the previous stationary value. Conversely, if the shear rate restarts suddenly in the direction opposite to its previous value, e.g.  $-\dot{\gamma}_0$ , experimental observations by Narumi et al. (2002), Fig. 3, showed that the particle pressure  $p_p$  progressively increases from zero to its previous stationary value while the shear stress  $\sigma_{xy}$  progressively decreases from zero to the opposite of its previous stationary value. As shown on Fig. 9, all these features are remarkably well captured by the present model.

The apparent viscosity of the suspension is defined as  $\eta_{app} = \sigma_{xy}/\dot{\gamma}$ . From (7e), we obtain:

$$\eta_{app}(\gamma) = K|\dot{\gamma}_0|^{n-1} + \eta_e \gamma_{e,xy}(\gamma) (\alpha + \beta \gamma_{e,xy}(\gamma)) \quad (17)$$

Notice that when  $n = 1$ , the apparent viscosity is independent of the shear rate, while

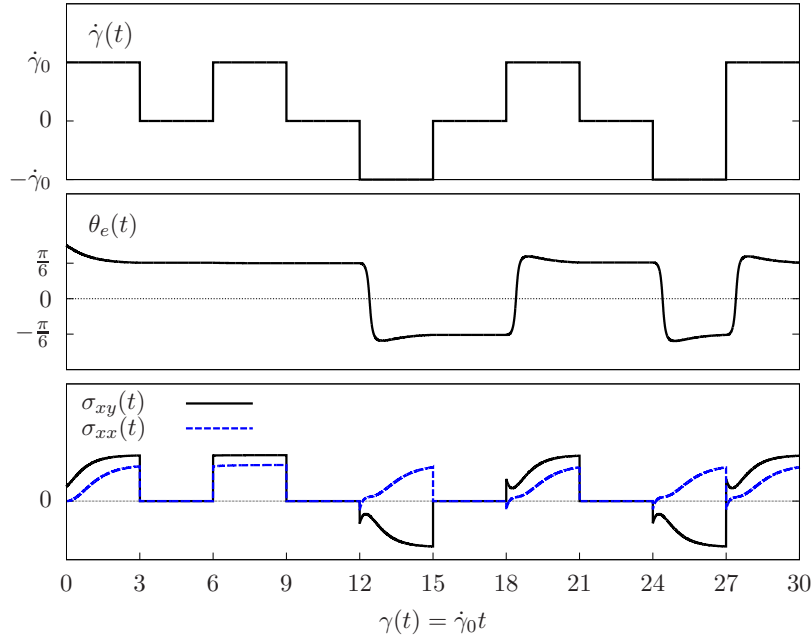


**FIG. 9.** Shear evolution with pauses, startups and reversals: evolution of imposed shear rate, depletion angle, and stress components versus shear deformation (choice of parameters:  $\alpha = \sqrt{3}$ ,  $\beta = 5$ ,  $\eta_e = 10$  Pa.s,  $K = 10$  Pa.s,  $n = 1$ ).

for slightly shear-thinning fluids, it would be slightly rate-dependent. Fig. 10 presents the evolution of apparent viscosity for a shear reversal, together with a sensitivity analysis to the model parameters. The apparent viscosity shows three regimes after the shear reversal: first, an instantaneous decrease is observed. The apparent viscosity then continues to decrease with a smooth shape until a minimum is reached. Finally, the apparent viscosity increases and relaxes exponentially to its stationary value. As shown in Fig. 10, these different regimes are diversely affected by the model parameters  $\alpha$ ,  $\beta$ ,  $\eta_e$  and  $K$ . The parameter  $\alpha$  controls the relaxation of the solution to its stationary value: the larger  $\alpha$ , the faster the solution reaches the stationary regime. In fact,  $\alpha^{-1}$  interprets as a characteristic deformation for reaching the stationary regime. The parameter  $\beta$  controls the existence of the smooth minimum and the shape of the curve around this minimum. When  $\beta = 0$ , there is no smooth minimum, and the apparent viscosity is monotonically increasing immediately after the shear reversal. The viscosity  $\eta_e$  influences the stationary plateau, while the minimum remains unchanged. Finally, the parameter  $K$  globally shifts the apparent viscosity: note that this effect is obvious when considering (17). The effect of  $0 < n < 1$  is similar to that of  $K$ , as it shifts the apparent viscosity.

## B. Comparison with experiments

We quantitatively compared our model to the unsteady shear flow experiments of Blanc (2011), sec 3.3 (see also Blanc et al. (2011a,b, 2013)). This author performed shear reversal experiments in a Couette rheometer. The suspensions were prepared with polymethyl methacrylate (PMMA) spherical particles in a Newtonian oil at various volume fractions  $\phi$  ranging from 0.30 to 0.50. The experiments were performed at an imposed torque whose value was adjusted in order to obtain, for each volume fraction, similar angular velocities in the stationary regime. All geometrical and material parameters of the experiments are summarized in Table I. In the investigated range of volume fraction, the suspension has

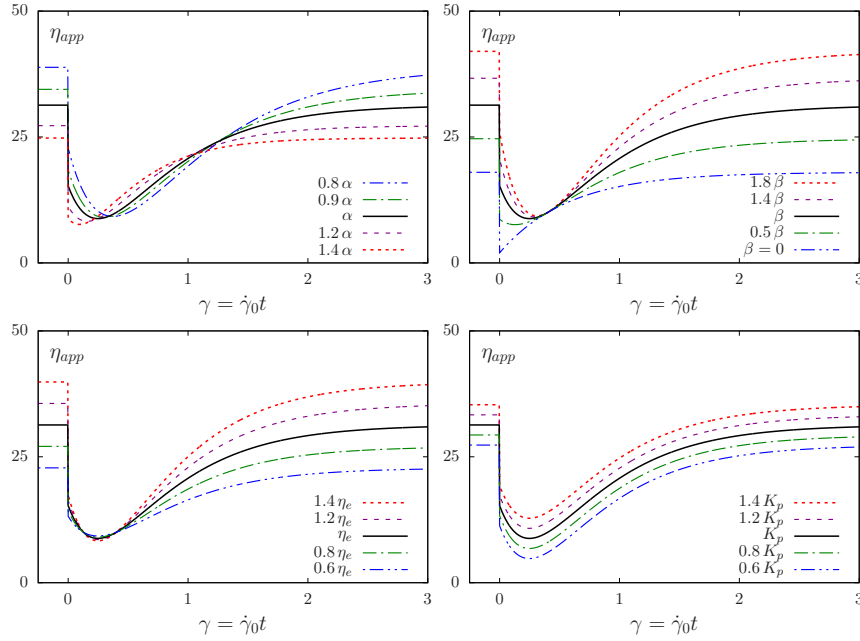


**FIG. 10.** Apparent viscosity during shear reversal: sensitivity of the response to the model parameters (base value of the parameters:  $\alpha = \sqrt{3}$ ,  $\beta = 5$ ,  $\eta_e = 10$  Pa.s,  $K = 10$  Pa.s<sup>n</sup>,  $n = 1$ ).

description	unit	symbol	value
fluid viscosity	Pa.s	$\eta_0$	1.03
power law index		$n$	0.9
outer radius	m	$R_e$	$2.4 \cdot 10^{-2}$
inner radius	m	$R_i$	$1.4 \cdot 10^{-2}$
height	m	$L$	$4.5 \cdot 10^{-2}$
torque	N.m	$T_m$	<i>imposed</i>
angular velocity	s <sup>-1</sup>	$\omega$	<i>measured</i>
shear stress	Pa	$\sigma_{r\theta}$	$\frac{0.818 \times T_m}{2\pi L R_c^2}$
shear rate	s <sup>-1</sup>	$\dot{\gamma}$	$\frac{\omega R_i}{R_e - R_i}$

**TABLE I.** Parameters of the shear reversal experiments of [Blanc \(2011\)](#).

been found slightly shear-thinning: the viscosity can be expressed by a power-law relation with a power index  $n = 0.9$ . This shear-thinning is interpreted as resulting from slight physico-chemical interactions (due to adsorbed polymers) between the particles. Neglecting the variations inside the gap, we assume the shear rate as uniform and consider this experiment as a simple shear flow. The problem is then described again by (7a)-(7f), where now  $\sigma_{xy}$  is imposed and  $\dot{\gamma}$  is unknown. Observe that, for  $n = 1$ , based on relation (7e), the unknown shear rate  $\dot{\gamma}$  expresses explicitly in terms of the unknown  $\gamma_{e,xy}$  and the given data  $\sigma_{xy}$ . This expression can then be inserted in (7a), yielding a nonlinear scalar ordinary differential equation for  $\gamma_{e,xy}$ . This equation does not admit, to our knowledge, an explicit solution and should be solved numerically. As in the previous paragraph, the numerical procedure uses `lsode` library ([Radhakrishnan and Hindmarsh, 1993](#)). In addition, when  $0 < n < 1$  as in the present case, the computation of the unknown shear rate  $\dot{\gamma}$  from (7e),



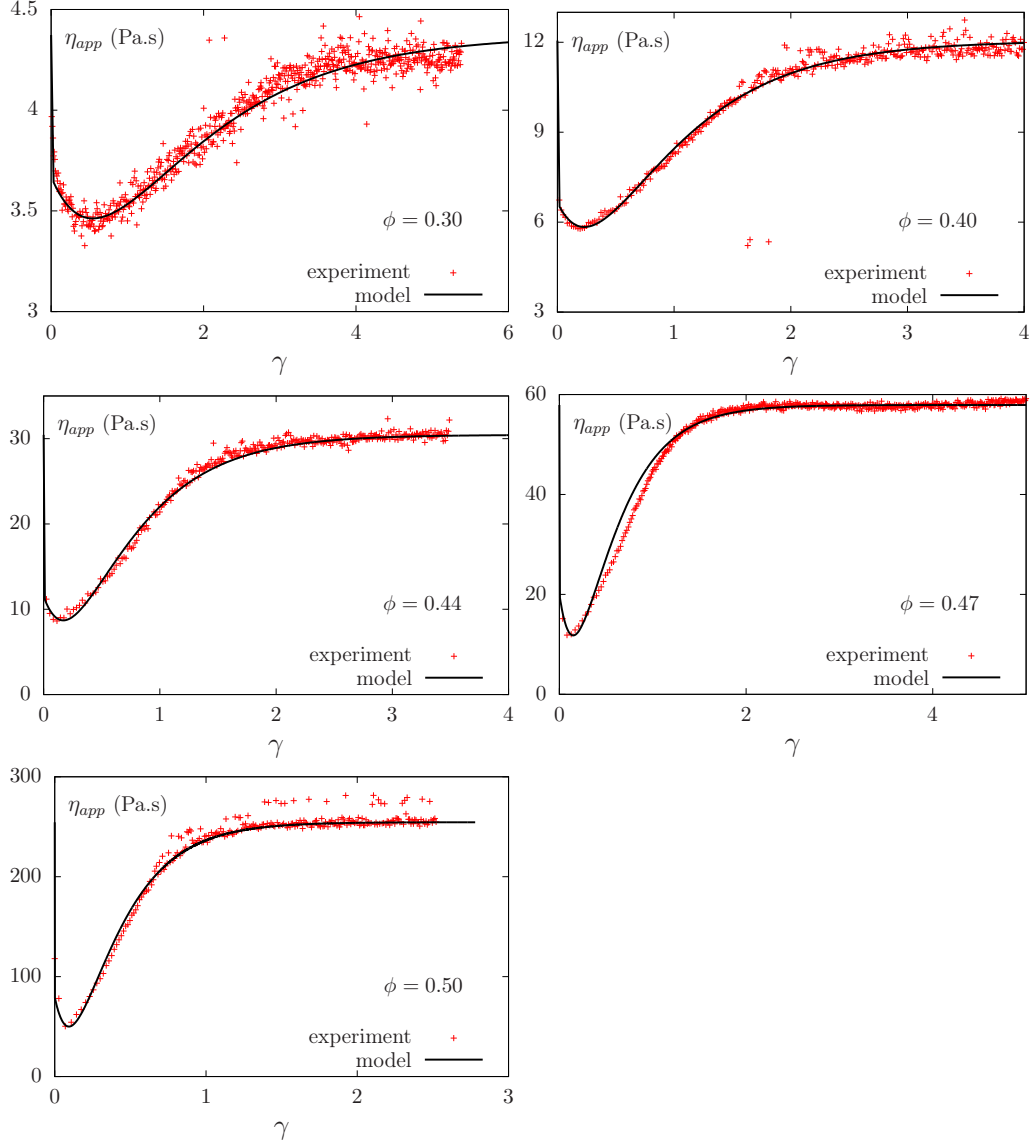


**FIG. 11.** Shear reversal: apparent viscosity  $\eta_{app}$  vs deformation  $\gamma$ . Comparison between experimental measurements (from [Blanc \(2011\)](#)) for a PMMA suspension in a Couette geometry and computations with the present model. For each volume fraction  $\phi$ , the three model parameters  $\lambda$ ,  $\eta_e$ ,  $K$  were obtained through a best-fit procedure. Parameter values are indicated in [Table II](#).

in terms of  $\gamma_{e,xy}$  and  $\sigma_{xy}$ , is performed numerically using a Newton method.

The present model contains four parameters that need to be determined:  $\alpha$ ,  $\beta$ ,  $\eta_e$  and  $K$ . The  $\alpha$  parameter has been already identified for this experimental setup, and its dependence upon  $\phi$  is given by (11). For each volume fraction, identification of the three others parameters can be performed based on the evolution of the apparent viscosity  $\eta_{app} = \sigma_{xy}/\dot{\gamma}$  during the shear reversals, as illustrated in the previous sensitivity analysis.

[Fig. 11](#) presents direct comparisons between model prediction and experimental measurements of the apparent viscosity. Observe that the sudden decrease of the apparent viscosity after shear reversal, and its relaxation to the stationary value, are qualitatively and quantitatively very well reproduced by the present continuous model, and this for the different volume fractions investigated. For  $\phi = 0.47$ , the apparent viscosity measured during the

$\phi$	$T_m$ ( $10^{-3}$ Nm)	$\alpha$	$\beta$	$\eta_e$ (Pa.s)	$K$ (Pa.s <sup>n</sup> )
0.30	0.07	0.715	0.719	0.32	2.95
0.40	0.10	1.33	1.88	2.5	5.3
0.44	0.25	1.80	3.37	8.9	9.4
0.47	0.50	2.37	6.78	18	14
0.50	2.00	3.38	10.3	88	67

**TABLE II.** Model parameters used to fit the experiments of [Blanc \(2011\)](#).

experiments displays a very slowly increasing trend for large deformations  $\gamma$ . This feature, which is obviously not captured by the model, could be due to slow migration of the particles induced by the small variations of the shear rate in the Couette gap.

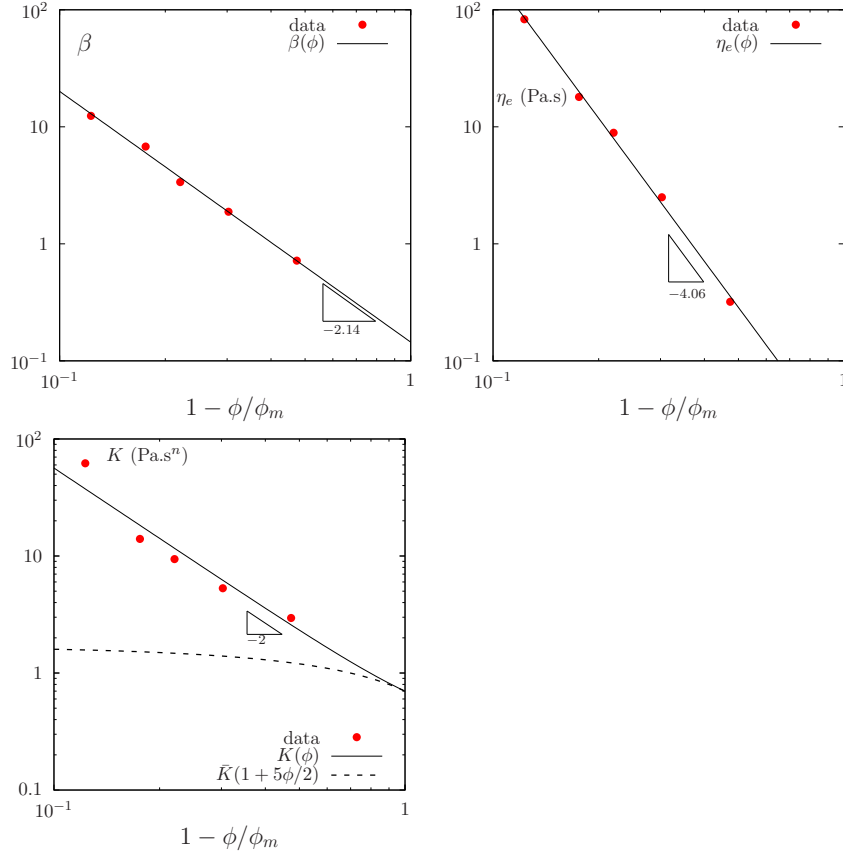


**FIG. 12.** Evolution with  $\phi$  of the model parameters  $\beta$ ,  $\eta_e$ , and  $K$ , and best fits provided by expressions (18a)-(18c).

Table II summarizes, for each volume fraction, the values of the four adjustable parameters  $\alpha$ ,  $\beta$ ,  $\eta_e$  and  $K$ . Fig. 12 shows the dependency upon  $\phi$  of the parameters  $\beta$ ,  $\eta_e$  and  $K$ . The regularity of these dependencies suggests the existence of material functions with the

$\phi_m$	$\delta_e$ (rad)	$\bar{\beta}$	$\nu_\beta$	$\bar{\eta}_e$ (Pa.s)	$\nu_e$
0.571	0.661	0.144	2.14	0.0171	4.06

$\bar{K}$ (Pa.s <sup>n</sup> )	$n$	$\nu$	$\omega$
0.670	0.9	2.00	0.807

**TABLE III.** Fitting parameters involved in expressions (11) and (18a)-(18c).

following forms:

$$\beta(\phi) = \bar{\beta} \left(1 - \frac{\phi}{\phi_m}\right)^{-\nu_\beta} \quad (18a)$$

$$\eta_e(\phi) = \bar{\eta}_e \left(1 - \frac{\phi}{\phi_m}\right)^{-\nu_e} \quad (18b)$$

$$K(\phi) = \bar{K} \left(1 - \omega + \left(\frac{5}{2} - \frac{\nu\omega}{\phi_m}\right) \phi + \omega \left(1 - \frac{\phi}{\phi_m}\right)^{-\nu}\right) \quad (18c)$$

Hence,  $\beta$  and  $\eta_e$  vs  $\phi$  are expressed by simple power-law dependencies diverging at  $\phi = \phi_m$ , where  $\phi_m$  is the maximum volume fraction of the suspension. Expression (18c) for  $K(\phi)$  is an original extension of [Krieger and Dougherty \(1959\)](#) law. The parameter  $\nu_\beta \approx 2$  corresponds to the power-law index of Krieger-Dougherty law, while  $\omega$  is a balance parameter. When volume fraction is small, the first order development of (18c) coincides with [Einstein \(1906\)](#) law  $K(\phi)/\bar{K} = 1 + 5\phi/2 + \mathcal{O}(\phi^2)$  for any value of  $\phi_m$ ,  $\nu_\beta \geq 0$  and  $\omega \in [0, 1]$ . Best-fitted values of all the material parameters involved in (18a)-(18c) are indicated in Table III.

## V. DISCUSSION AND CONCLUSIONS

This paper proposes a new tensorial model to describe the rheology of non-colloidal suspensions. In an attempt to clearly represent to role of microstructure, the contribution to the total stress of the suspension of local anisotropic particle arrangements, is accounted for through a specific *cluster stress*. This cluster stress is expressed as a function of a local conformation tensor whose evolution is governed by a rate-independent viscoelastic-like differential equation. Qualitatively, this model proves capable of reproducing all the main non-Newtonian trends exhibited by concentrated suspensions. First, the development of an anisotropic, and fore-aft asymmetric, microstructure in simple shear is well captured by the conformation tensor. As expected, the stationary microstructure is independent of shear rate (see (9)). The depletion angle, which corresponds to the largest eigenvalue of the the conformation tensor, is a function of a single model parameter  $\alpha$  that can be adjusted to fit experimental observations. Associated to the microstructure anisotropy, the model also predicts the existence of normal stresses and particle pressure that are proportional to shear rate. Regarding the shear stress, it can be made either linear with the shear rate (as expected in absence of colloidal effects), or non-linear to match the shear-thinning behavior observed in some experiments, depending on the power-index  $n$ . Second, in time-dependent cases, the model predicts transient responses associated to the progressive relaxation of the microstructure towards its stationary state. In agreement with experimental observations, these transient responses occur for shear reversals (due to the associated reversal of anisotropy direction), but not for changes of shear rate with the same sign (since microstructure is rate-independent). Also in agreement with experiments, the microstructure remains frozen during shear pauses, and its evolution during the transients is fully controlled by the shear deformation. The critical deformation to reach the stationary regime is directly related, again, to the parameter  $\alpha$ .

Overall, the model presented here includes only 5 constitutive parameters (only 4 if the shear-thinning parameter  $n$  is taken as fixed). Besides  $\alpha$ , two viscosities  $K$  and  $\eta_e$  represent the base viscosity of the suspension for an isotropic microstructure and the excess viscosity induced by microstructure anisotropy, respectively (note that  $K$  is rather a consistency if  $n < 1$ ), while the non-linearity parameter  $\beta$  controls the early stage of the transients. This limited number of parameters, and their clear physical meaning, is an advantage compared to most previous microstructure-based rheological proposed in the literature (Phan-Thien et al., 1999; Goddard, 2006; Stickel et al., 2006). Parameter identification for quantitative comparisons with experimental data, in particular, is relatively straightforward. Hence, we showed that the model is capable of quantitatively reproducing the complex transient evolution of apparent viscosity observed after shear reversals for a large range of volume fractions. Both the immediate response, characterized by an instantaneous drop followed by a smooth minimum, and the subsequent exponential relaxation, are well captured. Note that the quadratic term in (5), and the parameter  $\beta$ , are essential to obtain the smooth minimum observed in experimental data. Accounting for the quadratic term in (4), which has been neglected for simplicity in the computations presented above, would not alter the agreement with the data. When this term is reintroduced, the solution in simple shear is no longer explicit, but its numerical computation leads to similar results. To our knowledge, it is the first time that a microstructure-based rheological model is successfully compared to such a wide experimental dataset. This comparison allowed us to derive material functions for the evolution of the constitutive parameters with volume fraction. Noteworthily, the values of the parameter  $\alpha$  were determined from microstructure data (depletion angle), and then applied without adjustment to model the transient response. This validates the use of a single parameter controlling both microstructure anisotropy and the characteristic deformation during transients.

As a further quantitative validation, the model also proved capable of reproducing not only the depletion angle, but the shape of the first Fourier mode of the pair distribution function for sufficiently concentrated suspensions ( $\theta_e > 30^\circ$  typically). Here also, it is the first time, to our knowledge, that a continuous model is used to obtain detailed microstructural predictions in agreement with experimental data. Accounting for higher-frequency modes would further improve the prediction of the pair distribution function both for high and low values of the volume fraction, but would require the consideration of higher-order structure tensors in the model. Other promising prospects include the addition of a friction term to the cluster stress, which could prove important for modeling volume fractions close to  $\phi_m$  and/or experiments performed at imposed particle pressure (Boyer et al., 2011a). Future works will also consider more complex flows involving heterogeneous shear rates, such as Couette flows in large gap. In that case, through an approach analogous to what is classically done with SBM (Miller et al., 2009), our model could also be used to predict particle migration by considering the cluster stress  $\tau$  as the driver of the particle flux.

## ACKNOWLEDGEMENTS

It is a pleasure to thank Frédéric Blanc, Élisabeth Lemaire, Laurent Lobry and François Peters for fruitful discussions about the rheology of suspensions and for providing us data files of experimental measurements used in this paper for comparison with the present model.

## REFERENCES

- F. Blanc. *Rhéologie et microstructure des suspensions concentrées non browniennes*. PhD thesis, Université Nice Sophia Antipolis, 2011.
- F. Blanc, F. Peters, and E. Lemaire. Local transient rheological behavior of concentrated suspensions. *J. Rheol.*, 55(4):835–854, 2011a.

- F. Blanc, F. Peters, and E. Lemaire. Experimental signature of the pair trajectories of rough spheres in the shear-induced microstructure in noncolloidal suspensions. *Phys. Rev. Lett.*, 107(20):208302, 2011b.
- F. Blanc, E. Lemaire, A. Meunier, and F. Peters. Microstructure in sheared non-Brownian concentrated suspensions. *J. Rheol.*, 57(1):273–292, 2013.
- F. Boyer, É. Guazzelli, and O. Pouliquen. Unifying suspension and granular rheology. *Phys. Rev. Lett.*, 107(18):188301, 2011a.
- F. Boyer, O. Pouliquen, and É. Guazzelli. Dense suspensions in rotating-rod flows: normal stresses and particle migration. *J. Fluid Mech.*, 686:5–25, 2011b.
- J. F. Brady and J. F. Morris. Microstructure of strongly sheared suspensions and its impact on rheology and diffusion. *J. Fluid Mech.*, 348:103–139, 1997.
- É. Couturier, F. Boyer, O. Pouliquen, and É. Guazzelli. Suspensions in a tilted trough: second normal stress difference. *J. Fluid Mech.*, 686:26–39, 2011.
- T. Dbouk, L. Lobry, and E. Lemaire. Normal stresses in concentrated non-Brownian suspensions. *J. Fluid Mech.*, 715:239–272, 2013.
- A. Deboeuf, G. Gauthier, J. Martin, Y. Yurkovetsky, and J. F. Morris. Particle pressure in a sheared suspension: a bridge from osmosis to granular dilatancy. *Physical review letters*, 102(10):108301, 2009.
- M. M. Denn and J. F. Morris. Rheology of non-brownian suspensions. *Ann. Rev. Chem. Biomol. Eng.*, 5:203–228, 2014.
- G. Drazer, J. Koplik, B. Khusid, and A. Acrivos. Deterministic and stochastic behaviour of non-Brownian spheres in sheared suspensions. *J. Fluid Mech.*, 460:307–335, 2002.
- J. W. Eaton, D. Bateman, and S. Hauberg. *Octave: A high-level interactive language for numerical computations*. Free software foundation, 2011. <http://www.gnu.org/software/octave>.
- A. Einstein. Eine neue bestimmung der moleküldimensionen. *Ann. Phys. ser. 4*, 19:289–306, 1906.
- A. Einstein. *Investigation on the theory of the Brownian movement*. Dover, Mineola, NY, USA, 1956.
- F. Gadala-Maria and A. Acrivos. Shear-induced structure in a concentrated suspension of solid spheres. *J. Rheol.*, 24(6):799–814, 1980.
- S. Gallier, E. Lemaire, F. Peters, and L. Lobry. Rheology of sheared suspensions of rough frictional particles. *J. Fluid Mech.*, 757:514–549, 2014.
- J. D. Goddard. A dissipative anisotropic fluid model for non-colloidal particle dispersions. *J. Fluid Mech.*, 568:1–17, 2006.
- E. Guazzelli and J. F. Morris. *A physical introduction to suspension dynamics*. Cambridge University Press, UK, 2012.
- G. L. Hand. A theory of anisotropic fluids. *J. Fluid Mech.*, 13(1):33–46, 1962.
- M. A. Hulsen. A sufficient condition for a positive definite configuration tensor in differential models. *J. Non-Newton. Fluid Mechanics*, 38(1):93–100, 1990.
- R. Jackson. Locally averaged equations of motion for a mixture of identical spherical particles and a Newtonian fluid. *Chem. Engrg. Sci.*, 52(15):2457–2469, 1997.
- R. Jackson. *The dynamics of fluidized particles*. Cambridge University Press, UK, 2000.
- V. G. Kolli, E. J. Pollauf, and F. Gadala-Maria. Transient normal stress response in a concentrated suspension of spherical particles. *J. Rheol.*, 46(1):321–334, 2002.
- D. Kolymbas. An outline of hypoplasticity. *Arch. Appl. Mech.*, 61(3):143–151, 1991.
- I. M. Krieger and T. J. Dougherty. A mechanism for non-newtonian flow in suspensions of rigid spheres. *Trans. Soc. Rheol.*, 3(1):137–152, 1959.
- D. Lhuillier. Migration of rigid particles in non-Brownian viscous suspensions. *Phys. Fluids*, 21(2):023302, 2009.
- G. G. Lipscomb, M. M. Denn, D. U. Hur, and D. V. Boger. The flow of fiber suspensions in complex geometries. *J. Non-Newton. Fluid Mech.*, 26(3):297–325, 1988.
- B. Metzger and J. E. Butler. Irreversibility and chaos: role of long-range hydrodynamic interactions in sheared suspensions. *Phys. Rev. E*, 82(5):051406, 2010.
- R. M. Miller and J. F. Morris. Normal stress-driven migration and axial development in pressure-driven flow of concentrated suspensions. *J. Non-Newton. Fluid Mech.*, 135(2):149–165, 2006.
- R. M. Miller, J. P. Singh, and J. F. Morris. Suspension flow modeling for general geometries. *Chem. Eng. Sci.*, 64(22):4597–4610, 2009.
- J. F. Morris. A review of microstructure in concentrated suspensions and its implications for rheology and bulk flow. *Rheol. Acta*, 48(8):909–923, 2009.
- J. F. Morris and F. Boulay. Curvilinear flows of noncolloidal suspensions: the role of normal stresses. *J. Rheol.*, 43(5):1213–1237, 1999.
- T. Narumi, H. See, Y. Honma, T. Hasegawa, T. Takahashi, and N. Phan-Thien. Transient response of concentrated suspensions after shear reversal. *J. Rheol.*, 46(1):295–305, 2002.
- P. R. Nott and J. F. Brady. Pressure-driven flow of suspensions: simulation and theory. *J. Fluid Mech.*, 275:157–199, 1994.
- P. R. Nott, E. Guazzelli, and O. Pouliquen. The suspension balance model revisited. *Phys. Fluids*, 23(4):043304, 2011.
- J. G. Oldroyd. On the formulation of rheological equations of states. *Proc. R. Soc. Lond. A*, 200:523–541, 1950.
- N. Phan-Thien. Constitutive equation for concentrated suspensions in Newtonian liquids. *J. Rheol.*, 39(4):679–695, 1995.

- N. Phan-Thien, X.-J. Fan, and B. C. Khoo. A new constitutive model for monodispersed suspensions of spheres at high concentrations. *Rheol. Acta*, 38(4):297–304, 1999.
- N. Phan-Thien, X.-J. Fan, and R. Zheng. A numerical simulation of suspension flow using a constitutive model based on anisotropic interparticle interactions. *Rheol. Acta*, 39(2):122–130, 2000.
- K. Radhakrishnan and A. C. Hindmarsh. Description and use of LSODE, the Livermore solver for ordinary differential equations. Technical Report UCRL-ID-113855, LLNL, 1993.
- B. D. Reddy and G. P. Mitchell. Finite element analysis of fibre suspension flows. *Comput. Meth. Appl. Mech. Eng.*, 190(18):2349–2367, 2001.
- P. Saramito. *Complex fluids: modelling and algorithms*. Springer, 2016.
- J. J. Stickel and R. L. Powell. Fluid mechanics and rheology of dense suspensions. *Annu. Rev. Fluid Mech.*, 37:129–149, 2005.
- J. J. Stickel, R. J. Phillips, and R. L. Powell. A constitutive model for microstructure and total stress in particulate suspensions. *J. Rheol.*, 50(4):379–413, 2006.
- J. J. Stickel, R. J. Phillips, and R. L. Powell. Application of a constitutive model for particulate suspensions: time-dependent viscometric flows. *J. Rheol.*, 51(6):1271–1302, 2007.
- H. Troadec, F. Radjai, S. Roux, and J. C. Charmet. Model for granular texture with steric exclusion. *Phys. Rev. E*, 66(4):041305, 2002.
- T. Williams and C. Keley. `gnuplot`: an interactive program, 2010. <http://www.gnuplot.info>.
- K. Yapici, R. L. Powell, and R. J. Phillips. Particle migration and suspension structure in steady and oscillatory plane Poiseuille flow. *Phys. Fluids*, 21(5):053302, 2009.
- I. E. Zarraga, D. A. Hill, and D. T. Leighton Jr. The characterization of the total stress of concentrated suspensions of noncolloidal spheres in Newtonian fluids. *J. Rheol.*, 44(2):185–220, 2000.

## Appendix A: Computation of the probability distribution function

Let  $\mu_{\pm}$  be the two eigenvalues of the fabric tensor  $\langle \mathbf{n} \otimes \mathbf{n} \rangle$ , with  $\mu_- \leq \mu_+$  and  $\mathbf{e}_- = (\cos(\theta_e), \sin(\theta_e))$  and  $\mathbf{e}_+ = (-\sin(\theta_e), \cos(\theta_e))$ , the two corresponding eigenvectors, where  $\theta_e$  is the depletion angle. From the definition (12) of the average operator  $\langle \cdot \rangle$ , we have:

$$\int_{-\pi}^{\pi} \mathbf{n}(\theta) \otimes \mathbf{n}(\theta) p(\theta) d\theta = \langle \mathbf{n} \otimes \mathbf{n} \rangle$$

where  $\mathbf{n}(\theta) = (\cos \theta, \sin \theta)$  is the unit outward normal vector to the unit circle. The previous equation is then expressed in the eigenbasis. Observing that  $\mathbf{n} \cdot \mathbf{e}_- = \cos(\theta - \theta_e)$  and  $\mathbf{n} \cdot \mathbf{e}_+ = \sin(\theta - \theta_e)$ , we get:

$$\int_{-\pi}^{\pi} \cos^2(\theta - \theta_e) p(\theta) d\theta = \mu_- \quad (\text{A1a})$$

$$\int_{-\pi}^{\pi} \sin^2(\theta - \theta_e) p(\theta) d\theta = \mu_+ \quad (\text{A1b})$$

Note that, by construction,  $p(\theta)$  is even (see Fig. 4). Then, investigating  $p(\theta)$  by a Fourier series as:

$$p(\theta) = \sum_{k \geq 0} p_k \cos(2k(\theta - \theta_e))$$

where  $p_k \in \mathbb{R}$ ,  $k \geq 0$  are the Fourier coefficients, we obtain from (A1a)-(A1b), after computation of the integrals, that  $p_0 = 1/(2\pi)$  and  $p_1 = -(\mu_+ - \mu_-)/\pi$  while the coefficients  $p_k$  for  $k \geq 2$  remains still undetermined. Observe from Fig. 6 that these coefficients are strongly decreasing. By retaining only the two first coefficients, the present model is able to predict the following probability distribution:

$$p(\theta) = \frac{1}{2\pi} (1 - 2(\mu_+ - \mu_-) \cos\{2(\theta - \theta_e)\}) \quad (\text{A2})$$

Note that such expression was previously used by Troadec et al. (2002), eqn (1). Remark that  $\theta_e$  minimizes  $p(\theta)$ : the depletion angle is the direction where the probability to find a neighbor particle is minimal.



For the present model, the fabric tensor is expressed by  $\langle \mathbf{n} \otimes \mathbf{n} \rangle = \mathbf{b}_e / \text{tr } \mathbf{b}_e$  with  $\mathbf{b}_e = \mathbf{I} + \gamma_e$ . Then  $\mu_{\pm} = (1 + \lambda_{\pm}) / (2 + \lambda_+ + \lambda_-)$  where  $\lambda_{\pm}$  denotes the two eigenvalues of  $\gamma_e$ . From (8a), we have  $\lambda_{\pm} = (1 \pm \sqrt{1 + \alpha^2}) / \alpha^2$ . The previous relation (A2) writes explicitly in terms of the model parameter  $\alpha$  only as:

$$p(\theta) = \frac{1}{2\pi} \left( 1 - \frac{2}{\sqrt{1 + \alpha^2}} \cos(2(\theta - \theta_e)) \right) \quad (\text{A3})$$

where  $\theta_e$  is expressed explicitly versus  $\alpha$  by (9). Observe that  $p(\theta)$  remains in  $[0, 1]$  if and only if  $\alpha \geq \sqrt{3}$  which correspond to  $\theta_e \geq \pi/6$  and high volume fractions. Otherwise, for  $\alpha < \sqrt{3}$ , associated to  $\theta_e < \pi/6$  and dilute suspensions, the probability distribution function, as obtained from the present model, is not bounded in  $[0, 1]$ .